Enhanced Coulomb Counting Method for State-of-Charge Estimation of Lithium-ion Batteries based on Peukert's Law and Coulombic Efficiency

Jiale Xie[*], Jiachen Ma[†], and Kun Bai[**]

[†,*]School of Astronautics, Harbin Institute of Technology, Harbin, China
[**]State Grid Jibei Electric Power Co. Ltd., Maintenance Branch, Beijing, China

Abstract

Conventional battery state-of-charge (SoC) estimation methods either involve sophisticated models or consume considerable computational resource. This study constructs an enhanced coulomb counting method (Ah method) for the SoC estimation of lithium-ion batteries (LiBs) by expanding the *Peukert* equation for the discharging process and incorporating the Coulombic efficiency for the charging process. Both the rate- and temperature-dependence of battery capacity are encompassed. An SoC mapping approach is also devised for initial SoC determination and Ah method correction. The charge counting performance at different sampling frequencies is analyzed experimentally and theoretically. To achieve a favorable compromise between sampling frequency and accumulation accuracy, a frequency-adjustable current sampling solution is developed. Experiments under the augmented urban dynamometer driving schedule cycles at different temperatures are conducted on two LiBs of different chemistries. Results verify the effectiveness and generalization ability of the proposed SoC estimation method.

Key words: Coulomb counting, Coulombic efficiency, *Peukert's* law, State-of-charge

NOMENCLATURE

C_p	*Peukert* capacity
pc	*Peukert* coefficient
η	Coulombic efficiency
C_n, C_a	Nominal and actual capacity
T_n, I_n	Nominal temperature and current rate
$\Delta t, f_s$	Sampling interval and frequency
I_{eff}	Effective current
V_t	Battery terminal voltage
R_{in}	Battery internal resistance
$\Phi(T)$	Temperature correction term for discharging
$\Upsilon(I), \Upsilon(T)$	Correction terms on Coulombic efficiency
I_r, Q_r, T_r	Relative current, capacity, temperature

I. INTRODUCTION

Lithium-ion batteries (LiBs) are widely adopted in electric vehicles (EVs). Estimating the state-of-charge (SoC) is essential to a battery management system (BMS) for realizing efficient and safe operations [1]. To avoid being stranded halfway and relieve range anxiety [2], the SoC can be employed as a replacement for fuel gauges in conventional vehicles. Furthermore, real-time SoC monitoring can protect batteries from over-charge and over-discharge, which may cause permanent damage to the cell's internal structure [3]. Accordingly, unpredicted system interruptions can be reduced. However, SoC estimation is complicated because LiB behaviors strongly depend on operating conditions.

A. Review of SoC Estimation Methods

Open circuit voltage (OCV) is a readily acquired quantity employed for SoC evaluation [2], [4]. However, the pronounced hysteresis phenomenon and the very flat voltage plateau of LiFePO$_4$ batteries (LFPBs) [5] result in low-precision OCV-based methods [1]. Another battery feature, internal resistance, has also been exploited in the pursuit of

SoC through feature mapping. However, the irregular correlation between internal resistance and SoC also proves inappropriate for reliable SoC assessment [9]-[11].

Several validated battery models at various levels of abstraction, ranging in complexity from equivalent circuit models (ECMs) to multi-scale electrochemical simulations (ECSs), have been validated for SoC estimation [12], [13]. ECMs intuitively emulate battery electrical behaviors with an assembly of electric components, such as resistors and capacitors [1], [11], [14]. The interrelationships between internal states and external quantities can then be translated to mathematical expressions and conveniently combined with algorithms, such as Kalman filters [15]-[17] and other observer techniques [18]. However, these circuit-based models are generally simplified by ignoring notable features such as nonlinear equilibrium potential, rate-dependent capacity, and temperature effect [19]. Moreover, the high computational demands of these algorithms usually exceed the capability of on-board BMSs because of the large amount of matrix operations involved. ECSs attain satisfactory state evaluation by encompassing multiple physics and attributes, such as electrode geometry and electrolyte diffusion rate [20], [21]. However, the extensive calibration efforts should usually be repeated in case of chemistry or configuration change. Similarly, the great occupation of computational resources makes ECSs impractical for on-board applications.

Battery nonlinear characteristics can be reconstructed through the implementation of artificial neural network [22], fuzzy logic [23], and support vector machine [24] algorithms. However, these algorithms strongly depend on the quantity and quality of training data [10] and are sensitive to external disturbances. Importantly, the balance between under-fitting and over-fitting needs to be regulated empirically.

Physical probing techniques have also been explored. The ultrasonic waves transmitting across batteries are related to the porosity change of anode materials, which is used to infer the SoC in [25]. Correlating battery mechanical stress to graphite lithiation degree can likewise help determine the SoC [26]. In [27], the battery's magnetic characteristic is used as an SoC indicator. Although these techniques are promising, they require signals that are unavailable unless additional expensive sensors are installed.

Without intensive models or additional signals, the coulomb counting method (hereafter referred as the Ah method) calculates SoC directly by accumulating the inflow and outflow charges [28]. However, it suffers several widely acknowledged drawbacks [11]. First, the amount of charge that can be poured into and drawn out from a given battery varies significantly when it is subjected to temperature or load fluctuations. Second, the initial SoC should be provided by other auxiliary techniques. Finally, the accuracy is excessively reliant on precise current measurement because of an insufficient self-correcting capability.

B. Adaptions of the Ah Method

1) Peukert's Law

The discharge current rate exhibits a remarkable impact on the available capacity of a battery. To capture this rate-capacity characteristic, *Peukert's* law is originally introduced for lead–acid batteries in [29], in which the discharge capacity as a function of current density is formulated as

$$C_p = i^{pc} \cdot t \tag{1}$$

where C_p (constant for a given battery) is the *Peukert* capacity, t is the available discharge time, and pc is the *Peukert* coefficient. *Baert et al.* explained Eq. (1) with an electrochemical diffusion model [30]. *Doerffel et al.* extended Eq. (1) to LiBs and accomplished favorable results [31]. However, Eq. (1) requires the battery to be discharged strictly at nearly constant current and temperature [31], [32]. In hybrid EV situations, batteries not only go through a wide range of temperatures, but also experience dynamic load current, including different rates and charge/discharge alternations [33]. Variable load and temperature pose challenges to *Peukert's* law and may result in errors of up to 20% [34]. Although *Austin et al.* expanded Eq. (1) by factoring in different discharge rates and temperatures, they ignored the charging behavior [20]. Given that *Peukert's* law only applies to discharging, Eq. (1) cannot address driving scenarios, including regenerative braking. Therefore, a complementary technique should be incorporated for the charging process.

2) Coulombic Efficiency

For a given battery, the releasable charge is always less than the stored charge during an operation cycle. This effect is denoted as the Coulombic efficiency (η), by which the current in the Ah method is usually multiplied as a correction [11]. The calibration of η is complex because both temperature and current rate influence it [8]. η is near 1 at low rates and declines at high rates due to the significant internal loss by secondary reactions. *Kong et al.* investigated the correlation between η and SoC [2]. However, they only focused on the variable discharging rates with the charging rate fixed and the influence of temperature ignored. *Feng et al.* considered current rate and temperature based on a large measurement matrix of different rates and temperatures to cover all possible operating conditions [7].

C. Contributions of This Study

Essentially, both *Peukert's* law and Coulombic efficiency transform the actual current into an effective form. This study enhances the traditional Ah method by combining an expanded *Peukert's* law for the discharging process and an elaborate Coulombic efficiency for the charging process. The rate- and temperature-dependence of capacity are factored in, whereby the current accumulative error is significantly reduced. An SoC mapping approach for initial SoC determination and self-correction is also introduced. Furthermore, the impact of
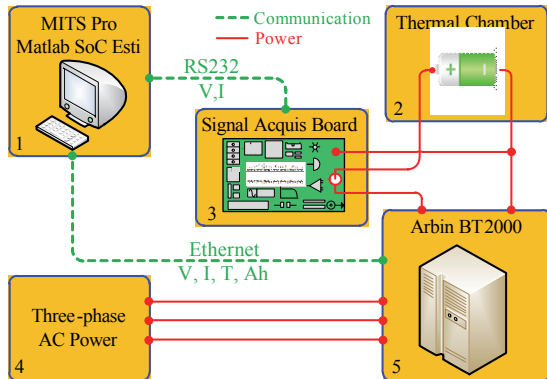
Fig. 1. Experimental system.

Fig. 2. Investigated batteries in this work.

TABLE I
SPECIFICATIONS OF THE INVESTIGATED BATTERIES

Parameter	Battery1	Battery2
Chemistry	LFP	LNCM
Nominal capacity (Ah)	20	25
Nominal discha current (C)	1/3	1/3
Upper cut-off voltage (V)	3.6	4.2
Lower cut-off voltage (V)	2.5	2.8
Max discharge current (C)	5	4
Max charge current (C)	1	1
Operating temperature (°C)	–20 to 45	–10 to 50

the current sampling frequency on charge counting accuracy is experimentally investigated and theoretically analyzed. In response, a frequency-adjustable (FA) current sampling solution is proposed to achieve balance between computational overhead and accumulation accuracy.

D. Organization of This Paper

Section II presents the testing equipment and investigated batteries. Section III illustrates the procedures of identifying pc and η under different conditions and the SoC mapping approach. Section IV presents the designed FA sampling solution. Section V provides the experimental results on two LiBs under various conditions to verify the enhanced SoC estimator. Finally, Section VI concludes this paper.

II. EXPERIMENTAL FACILITIES

As shown in Fig. 1, the test bench consists of a host PC, a battery tester Arbin BT2000, a thermal chamber, and a

Matlab-based SoC estimation algorithm. The accompanying softwares of BT2000, MITS Pro are also installed on the PC. To implement the FA sampling proposed in Section IV, a signal acquisition board is designed based on the chip LTC6803. The voltage measurement accuracy is 1.2 mV, and the on-chip 16-bit ADC is utilized for current sense. Two LiBs are investigated as shown in Fig. 2, and the specifications are tabulated in Table I. Battery1 is the sample for method elucidation, and then both Battery1 and Battery2 are used for method verification. During the tests, the batteries are always contained in the thermal chamber. The test procedure is suspended when the sensed temperature deviation from the preset temperature exceeds 2 °C. The commonly used OCV is not involved in this work. Thus, the time-consuming relaxation for voltage recovery is unnecessary, and the characteristic tests take significantly less time. Alternatively, the real-time terminal voltage (V_t) is adopted by continuously discharging the battery. To generalize the proposed method to different battery capacities, all currents are denoted in C-rate [33]. The aging effect is outside the scope of this paper, and all tests are conducted at a specific aging level.

III. ENHANCED COULOMB COUNTING METHOD

Battery capacity varies with the working condition. For example, extra energy can be extracted from a battery depleted at low temperature when it warms up; an exhausted battery discharged at high rates still has extractable capacity at low rates [31]. The present work assumes that a fully charged battery always holds a constant capacity C_n regardless of the working condition, whereas the specific condition influences the action effect of the current. Accordingly, a concept of effective current is proposed, and the SoC variation is calculated as

$$\Delta SoC = \frac{(I \cdot C_n) \cdot \Delta t}{C_a} = \frac{(I_{eff} \cdot C_n) \cdot \Delta t}{C_n} \qquad (2)$$

where I is the actual current, I_{eff} is the corresponding effective current of I, Δt is the sampling interval, C_a is the actual capacity, and C_n is the nominal capacity. Given that I and I_{eff} are denoted in C-rate, the respective currents in *Ampere* are $I \cdot C_n$ and $I_{eff} \cdot C_n$, respectively. From Eq. (2), I_{eff} is transformed as

$$I_{eff} = I \frac{C_n}{C_a}. \qquad (3)$$

In the following sections, I_{eff} is separately derived for the discharging and charging processes. The employed data are measured on Battery1. In this work, the nominal condition ($I_n = C/3$, $T_n = 23$ °C) under which the nominal capacity C_n can be obtained is regarded as the reference condition.

A. Peukert Equation for Discharging

To encompass the rate- and temperature-dependence of capacity, the effective current for discharging is defined as

$$I_{eff}(I,T) = I_{eff}(I) \cdot \Phi(T), \qquad (4)$$

where I is the actual current, $I_{eff}(I)$ is the underlying effective current, and $\Phi(T)$ is the temperature correction term.

1) Rate-dependence of Peukert Coefficient

From Eq. (1), $I_{eff}(I)$ can be deduced as (Appendix A)

$$I_{eff}(I) = I \cdot (I/I_n)^{pc-1}. \qquad (5)$$

Conventionally, static OCV–SoC correlations are used for capacity analysis and measured by inserting an interruption of several hours in-between every, for example, 5% SoC. However, this interruption is inconsistent with realistic driving situations and may obviously increase the released capacity. In our work, dynamic $V_t - Ah$ curves by continuous discharging are utilized to identify the pc, as illustrated in Fig. 3, where the data were acquired at $T_n = 23\ ^\circ$C. The reference curve L1 (black with squares) is discharged at $I_n = C/3$ and provides an actual nominal capacity, $C_n = 20.28Ah$. L2 (green dash) is the fourth-order polynomial fit of L1. L4 (red with solid circles) is discharged at $I = 0.1C$, for which the pc is to be extracted, and has a bigger capacity, $Q_b = 21.34Ah$.

Resulting from the battery internal resistance (R_{in}), V_t, which is monitored against the cut-off thresholds, shows a difference at different load currents though holding identical SoC. This outcome is mainly ascribed to the different potential drops on R_{in}. Thus, the larger the current applied on the battery, the earlier the cut-off voltage is reached, though the battery is not really exhausted. Consequently, inferring the pc using C_n and Q_b is not rigorous.

To eliminate the difference in potential drop on R_{in}, a blue dashed curve L3 is obtained by removing the excess internal loss from the reference curve L2, that is, dragging L2 upwards a distance, ΔH, which is theoretically regarded as the difference of V_t at the initial discharge moment, i.e., $R_{in}C_n(I_n - I)$ [6]. Furthermore, L3 is extrapolated down to the horizontal axis (low cut-off threshold), and a pseudo capacity of $Q_a = 20.51Ah$ is obtained. Then, the pc for $0.1C$ relative to $C/3$ can be calculated as (Appendix B)

$$pc = 1 + \frac{ln(Q_b/Q_a)}{ln(I_n/I)}. \qquad (6)$$

Similarly, the pc regarding discharge rates larger than $C/3$, such as $1C$, can be calculated with L5 and L6. The results of extracting the pc for other rates of $0.05C$, $0.2C$, $0.5C$, $1.5C$, $2C$, and $3C$ are shown in Fig. 4.

The correlation between pc and discharge rate is then fitted with the Matlab *Curve Fitting Toolbox*. Linear fitting, polynomial fitting, and exponential fitting are performed. The resultant indexes of the *Mean* and *Root-Mean-Square* (RMS) errors indicate that exponential approximation can best represent the rate-dependence of the *Peukert* coefficient as
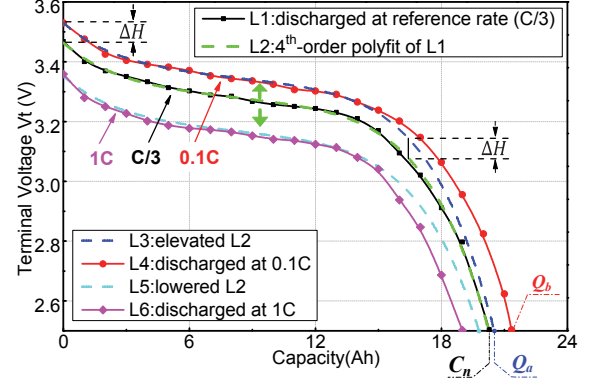

Fig. 3. Schematic of identifying the *Peukert* coefficient at different discharge rates.
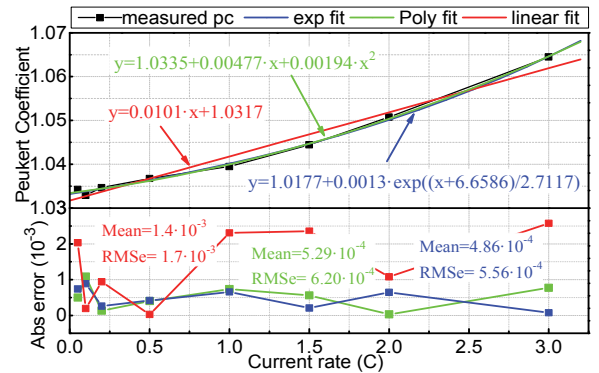

Fig. 4. Approximating the resultant *Peukert* coefficients with linear, polynomial, and exponential fittings, respectively.

$$pc(I) = a_I^p + b_I^p \cdot exp\big((I - \lambda_I^p)/\tau_I^p\big) \qquad (7)$$

where a_I^p, b_I^p, λ_I^p, and τ_I^p are fitted as 1.0177, 0.0013, −6.6585, and 2.7117, respectively.

Several similar fitting operations exist in the subsequent work, and they are all performed by selecting the fit form with the best performance in terms of accuracy and complexity.

2) Temperature-dependence of Peukert Coefficient

The temperature-dependence of capacity is considered by introducing a correction term $\Phi(T)$, which can be determined through a procedure similar to that in the last section. In this section, the battery is discharged at a fixed rate of $I_n = C/3$ under different temperatures. In Fig. 5(a), L1 (black with squares) is obtained under $T_n = 23\ ^\circ$C, and L2 (green dash) is its fourth-order polynomial fit. L4 (red with solid circles) is discharged under $0\ ^\circ$C, for which $\Phi(T)$ is sought, and has a capacity of $Q_c = 17.52Ah$. L3 (blue dash), which has a capacity of $Q_d = 19.37Ah$, is obtained by moving L2 a vertical displacement downward to achieve the best overlap with the flat portion of L4.

A visual illusion that decreasing L2 obtains L4 rather than L3 may occur. Fig. 5(b) presents a concise view of Fig. 5(a) by removing irrelevant elements. Shifting L2 to a consistent vertical distance ΔV_1 clearly achieves L3, whereas the
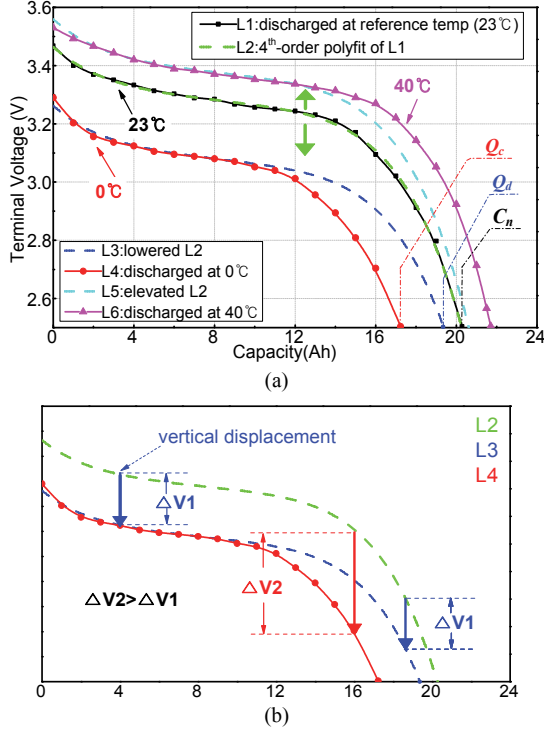
Fig. 5. (a) Schematic of identifying relative capacity under different temperatures, (b) a concise view of (a).
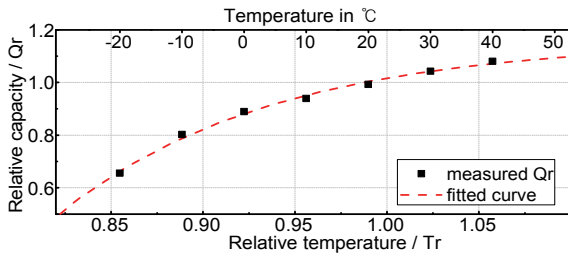

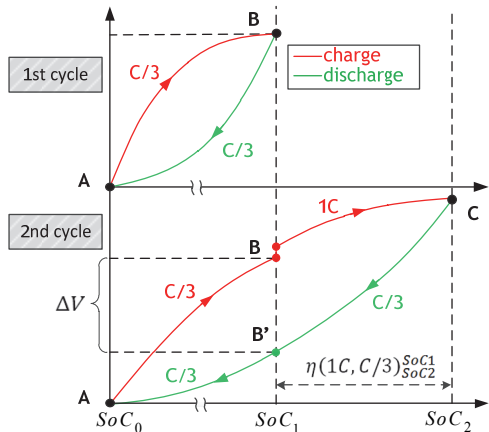Fig. 6. Resultant relative capacities and the fitted curve.

Fig. 7. Procedure for Coulombic efficiency identification.

obviously inconsistent distances of ΔV_1 and ΔV_2 are required to reach L4. The increasing deviation between L3 and L4 from capacity = 12Ah results from the different remaining capacities of L3 and L4. L3 has a large remaining

TABLE II
COMPARING THE INCORPORATED AND MEASURED EFFECTIVE CURRENT

Discharge Rate (C)	Temp (°C)	$I_{eff}(I,T)$ (C)	
		Incorporated	Measured
−0.6	−14	0.8254	0.8093
−0.6	38	0.5749	0.5711
−1.1	−12	1.5073	1.5253
−1.1	32	1.1009	1.1249
−1.8	−11	2.5092	2.4941
−1.8	27	1.8904	1.9297
−2.6	−5	3.4941	3.4411
−2.6	25	2.8595	2.7765
			RMSe = 0.0425

capacity and a long discharge time because its high internal resistance at low temperature causes severe energy loss.

Then, a dimensionless relative capacity, Q_r, is defined as

$$Q_r = Q_c/Q_d. \tag{8}$$

By setting T = −20 °C, −10 °C, 0 °C, 10 °C, 20 °C, 30 °C, and 40 °C, we identify Q_r as shown in Fig. 6, where T_r is the relative temperature:

$$T_r = (T + 273)/(T_n + 273). \tag{9}$$

The $Q_r - T_r$ correlation in Fig. 6 is fitted as

$$Q_r(T) = a_T^p + b_T^p \cdot ex\, p(-T_r/\tau_T^p), \tag{10}$$

where a_T^p, b_T^p, and τ_T^p are 1.158, −768.761, and 0.116, respectively.

Given that a high temperature results in a small releasable capacity, by referring to Eq. (3), we can say that high temperature leads to low effective current and vice versa. An opposite temperature effect should be equivalently imposed on I_{eff} because the battery is assumed to hold a fixed capacity, C_n. Thus, the reciprocal of $Q_r(T)$ can be treated as the temperature correction term in Eq. (4) as

$$\Phi(T) = 1/Q_r(T). \tag{11}$$

3) Verification of the Incorporated Effective Current

To verify the proposed effective current form in Eq. (4), eight other effective currents are measured and compared with the incorporated effective currents. As tabulated in Table II, the incorporated $I_{eff}(I,T)$ can basically capture the underlying trend of the actual effective current.

B. Coulombic Efficiency for Charging

Three factors, that may potentially influence the charging efficiency η, namely, current rate, SoC, and temperature, are considered. These factors are first studied experimentally and then the negligible one/ones are excluded. During charging, I_{eff} can be obtained using η according to different conditions as follows:

$$I_{eff}(SoC, I, T) = I \cdot \eta(SoC, I, T). \qquad (12)$$

Therefore, an accurate $\eta(SoC, I, T)$ is crucial. In this section, correlations $\eta - SoC$, $\eta - I$, and $\eta - T$ are first identified by keeping the other two factors at particular levels. Then, they are incorporated as $\eta(SoC, I, T)$.

1) Rate-Dependence of Coulombic Efficiency

Six charge rates, $0.05C$, $0.1C$, $C/3$, $0.5C$, $0.8C$, and $1C$, are considered, with $C/3$ as the reference discharge rate. The other two factors are kept at $T_n = 23\ °C$ and SoC = 50%–60%. To eliminate accidental disturbances, every test is performed four times, that is, four ηs are obtained for each rate. The one with the greatest deviation from the others is ignored and then the average is adopted. Taking the $1C$ charge for example, Fig. 7 illustrates the procedure to identify η as follows:

(1) An exhausted battery is charged at $C/3$ to $SoC_1 = 50\%$, that is, from A to B in the first cycle.
(2) The battery is discharged at $C/3$ to the lower cut-off voltage, that is, from B to A in the first cycle.
(3) Again, the battery is charged at $C/3$ to point B, that is, from A to B in the second cycle.
(4) The battery is continuously charged at $1C$ to $SoC_2 = 60\%$, that is, from B to C in the second cycle.
(5) The battery is discharged at $C/3$ to the lower cut-off voltage, that is, from C to A in the second cycle.

The η for the $1C$ charge rate test (relative to $C/3$ discharge) is calculated as

$$\eta(1C, C/3) = \frac{Q_{dis,C \to A}^{C/3,2nd} - Q_{dis,B \to A}^{C/3,1st}}{Q_{ch,B \to C}^{1C,2nd}} \qquad (13)$$

where the involved notations are explained in Table III. The η for the other charge rates can be obtained similarly.

Afterward, the above procedure is performed for two other SoC ranges: 20%–30% and 80%–90%. A relative Coulombic efficiency is defined as

$$Y(I) = \frac{\eta(I, C/3)}{\eta(C/3, C/3)}. \qquad (14)$$

The obtained $Y(I)$ is shown in Fig. 8. Then, a second-order polynomial fit is performed on the average points during each SoC range as

$$Y(I) = \sum_{\kappa=0}^{2} a_I^{\eta}(\kappa) \cdot I^{\kappa} \qquad (15)$$

where $a_I^{\eta}(\kappa)$ is identified as 1.00336, 0.00272, and −0.03936 for $\kappa = 0, 1, 2$, respectively. Then, $Y(I)$ can be regarded as a correction term that represents the influence of the current rate on η.

The respective voltages during the charging and discharging processes are significantly different due to the hysteresis potential and internal loss, such as the ΔV between B and B' in the second cycle of Fig. 7. Consequently, pinpointing B' using the terminal voltage is impractical when successive

TABLE III
MEANING OF THE NOTATIONS IN EQ. (13).

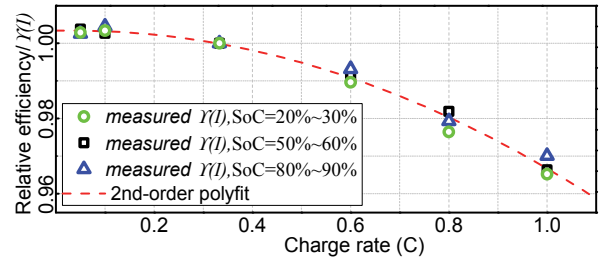| Notation	Meaning
$Q_{dis,B \to A}^{C/3,1st}$	the amount of charge drawn from the cell from B to A at $C/3$ in the first cycle
$Q_{ch,B \to C}^{1C,2nd}$	the amount of charge poured into the cell from B to C at $1C$ in the second cycle
$Q_{dis,C \to A}^{C/3,2nd}$	the amount of charge drawn from the cell from C to A at $C/3$ in the second cycle

Fig. 8. Resultant relative Coulombic efficiency $Y(I)$ and the fitted curve.
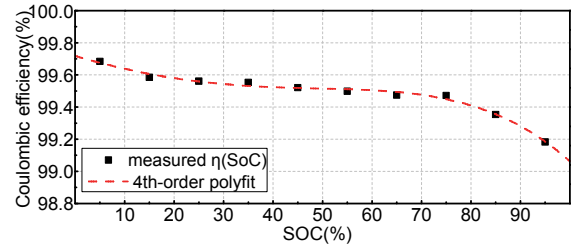

Fig. 9. Resultant Coulombic efficiency $\eta(SoC)$ within different SoC ranges and the fitted curve.
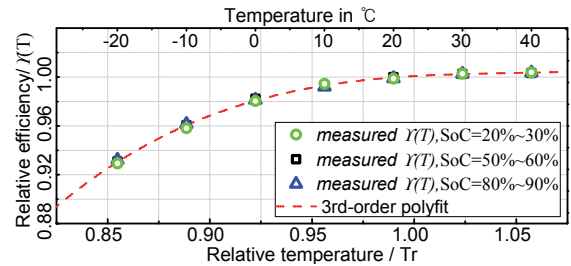

Fig. 10. Resultant relative Coulombic efficiency $Y(T)$ under different temperatures and the fitted curve.

charging and discharging are applied. In other words, aligning B' to B horizontally through discharging is infeasible. Meanwhile, a slight difference in charge throughput will lead to a considerable deviation on resultant η. Therefore, the battery should be charged or discharged consecutively, as detailed in Fig. 7, to avoid the negative influence of hysteresis and internal loss.

2) SoC-Dependence of Coulombic Efficiency

Since η has a remarkable dependence on SoC [8], an elaborate experimental analysis is necessary. Here, the entire SoC range (0%–100%) is evenly divided into 10 subsections,

TABLE IV
COMPARING THE INCORPORATED AND MEASURED $\eta(SoC, i, T)$.

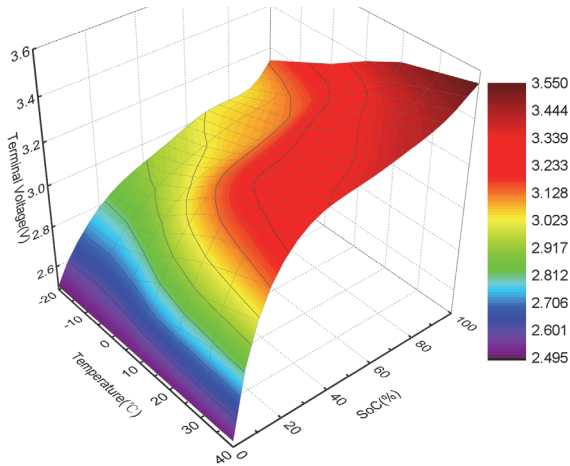| Charge Rate (C)	Temp (°C)	SoC (%)	$\eta(SoC, I, T)$	
			Incorporated	Measured
0.25	−14	37	94.688	94.653
0.25	−14	77	94.614	94.628
0.25	38	37	100.028	100.051
0.25	38	77	99.950	99.963
0.85	−8	37	93.893	94.013
0.85	−8	77	93.820	93.873
0.85	32	37	97.529	97.454
0.85	32	77	97.453	97.497
				RMSe = 0.0620

Fig. 11. $T - V_t^{C/3} - SoC$ correlation, where $V_t^{C/3}$ is the real-time terminal voltage by $C/3$ discharging.

which are investigated separately, referring to the procedure in Fig. 7. In this section, η is measured under $T_n = 23$ °C using $I_n = C/3$ as both charge and discharge rates. Fig. 9 presents the η obtained within different SoC subsections. Fitting the result with polynomials, the error decreases to an acceptable level when the order increases to fourth as

$$\eta(SoC) = \sum_{\kappa=0}^{4} a_{SoC}^{\eta}(\kappa) \cdot SoC^{\kappa} \qquad (16)$$

where $a_{SoC}^{\eta}(\kappa)$ are 99.718, $-8.88 \cdot 10^{-3}$, $8.285 \cdot 10^{-5}$, $1.14 \cdot 10^{-6}$, and $-1.736 \cdot 10^{-8}$ for $\kappa = 0, \cdots, 4$, respectively.

3) Temperature-Dependence of Coulombic Efficiency

To explore the temperature-dependence of η, a series of tests under $T = -20$ °C, -10 °C, 0 °C, 10 °C, 20 °C, 30 °C, and 40 °C in three SoC ranges of 20%–30%, 50%–60%, and 80%–90% are conducted. The detailed procedure is similar to that in Fig. 7, while $I_n = C/3$ is used as both charge and discharge rate. As Fig. 10 depicts, temperature has an evident influence on the relative Coulombic efficiency

$$Y(T) = \frac{\eta(T)}{\eta(23°C)}. \qquad (17)$$

Then, a third-order polynomial fit is performed on the average points in each SoC range as follows:

$$Y(T) = \sum_{\kappa=0}^{3} a_T^{\eta}(\kappa) \cdot T_r^{\kappa} \qquad (18)$$

where $a_T^{\eta}(\kappa)$ are −9.4219, 29.7226, −28.2756, and 8.9756 for $\kappa = 0, \cdots, 3$, respectively, and T_r is the relative temperature defined in Eq. (9). Here, $Y(T)$ is regarded as a correction term for η to adapt to different temperatures.

4) Verification of the Incorporated Coulombic Efficiency

From the tests above, SoC, current rate, and temperature all have significant impacts on η. Taking $\eta(SoC)$ as the underlying efficiency, $Y(I)$ and $Y(T)$ are regarded as correction terms. Thus, the final Coulombic efficiency is incorporated as

$$\eta(SoC, I, T) = \eta(SoC) \cdot Y(I) \cdot Y(T) \qquad (19)$$

Eight other Coulombic efficiencies under different conditions are measured and compared with the incorporated $\eta(SoC, I, T)$. The tests are conducted over the range of $\pm 5\%$ around the specified SoC level, such as the η at SoC = 37%, which is obtained from 32% to 42%. Table IV shows that the measured results have good consistency with the incorporated ones. The $RMSe$ suggests that the incorporation of the Coulombic efficiency is effective.

C. SoC Mapping during System Idles

When a fully charged battery is unavailable, the initial SoC is normally mapped from the OCV or memorized from last usage. Moreover, the Ah method requires periodic self-corrections to eliminate accumulated errors. However, OCV-based methods require a circuit-break relaxation to achieve the equilibrium state. The pronounced hysteresis potential for LFPBs should also be solved. After a long dormancy, the memorized SoC will lose efficacy because of the self-discharge effect. Here, we propose a SoC determination approach for the initialization and correction of the Ah method.

First, a series of tests is mandatory to draw the correlation of $T - V_t^{C/3} - SoC$, where T is the battery temperature, and $V_t^{C/3}$ is the terminal voltage at $C/3$ discharging (Fig. 11). Second, when the BMS launches or the system idles (e.g., waiting for the red traffic light), a 20-s $C/3$ discharge pulse is performed to achieve complete hysteresis. The V_t at the final moment of the discharge pulse is used to map the SoC from Fig. 11. The hysteresis potential has a quantitative relation with the charge throughput [35], [36]. If the charge throughput of the 20-s $C/3$ pulse exceeds that of the preceding regenerative pulse, then complete hysteresis can be achieved. Referring to the Federal Urban Driving Schedule [37], the 20-s C/3 pulse can accommodate 95% of the regenerative braking cases. Therefore, this approach can be implemented in most scenarios during actual driving. If a remarkable regenerative pulse occurs, the 20-s C/3 pulse can be delayed for a moment of driving and then employed to map the SoC.

Afterward, the estimation task is taken over by the enhanced Ah method described. This procedure takes about

20 s, neither delaying the driving nor bringing significant loss to the remaining capacity. The mapped SoC can be employed either as a correction or as the initial SoC for the Ah method.

IV. INFLUENCE OF SAMPLING RATE

Generally, the urban dynamometer driving schedule (UDDS) time–velocity cycle is misused as a time–current profile. A differential operation on the original UDDS cycle generates a time–acceleration profile, as Fig. 12 depicts. According to our knowledge of electrical machinery, we know that

$$\text{Acceleration} \propto \text{Torque} \propto \text{Current} \qquad (20)$$

where ∝ means directly proportional. Therefore, the time–acceleration profile can be physically deemed as a time–current profile, which is called UDDS-b in this paper. Fig. 12 indicates that UDDS-b is more dynamic and includes sharp accelerations and abrupt regenerative breakings, thereby simulating urban driving more realistically. Furthermore, to traverse the entire SoC range, an augmented segment of 360-s $1C$ discharge to reduce the SoC by 10% is attached in front of the UDDS-b. This profile is called augmented UDDS-b.

Thereafter, a series of charge counting tests at different current sampling frequencies (f_s = 0.04, 0.06, 0.1, 0.2, 0.4, 0.8, 1, 2, 4 Hz) is carried out. Fig. 13 shows the accuracy indexes, *Mean* error, and *Max* error after 10 UDDS-b cycles. At the lowest sampling frequency, f_s =0.04 Hz, the *Mean* error and *Max* error are higher than 10%. By boosting f_s to 0.06 Hz, the accuracy is sharply improved. An obvious inflection point occurs at f_s = 0.2 Hz, from which the *Mean* and *Max* errors decrease gradually as f_s increases. This accuracy evolution is analyzed as follows.

A 1369-point (UDDS-b data length), 1 Hz sampling frequency (UDDS-b time interval) fast Fourier transform (FFT) is performed on UDDS-b to draw its frequency spectrum (Fig. 14). The amplitude peaks at 0.025 Hz and then declines gradually until the harmonics higher than 0.2 Hz are negligible. The main frequency components, which have primary contributions to the detail of UDDS-b, spread across 0.02– 0.04 Hz. According to the theorem of *Shannon* sampling, which states that a sequence of twofold-rate samples can capture all the information of the original signal, samples lower than $2 \cdot 0.02$ Hz are insufficient for reconstructing the characteristics of UDDS-b with high fidelity. As f_s increases from 0.04 Hz to 0.1 Hz, the main frequency components are increasingly covered, thus improving the charge counting accuracy.

As stated, the determination of optimal sampling frequency requires prior knowledge of the load frequency spectrum. However, the load current is unpredictable and depends on real-time road conditions. In other words, a predetermined fixed sampling frequency makes no sense. In our work, a FA current sampling solution is proposed. As illustrated in Fig. 15, a differentiator is designed to perform a differential operation on the sensed current signal (preprocessed by
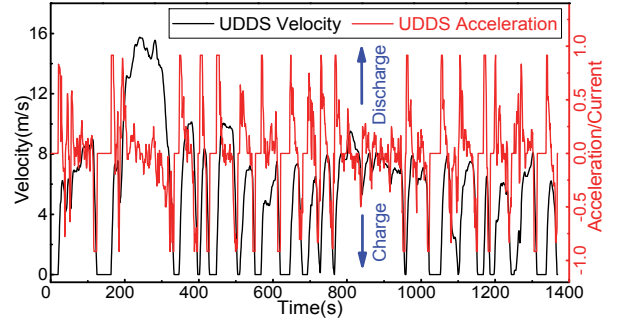

Fig. 12. Original UDDS time–velocity profile (black) and the UDDS-b time–acceleration/current profile (red).
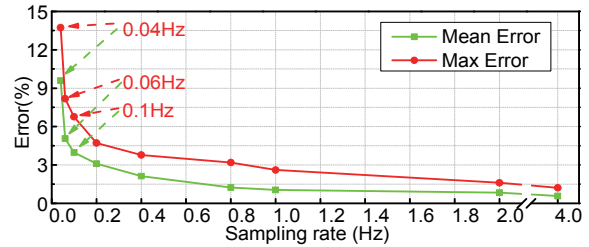

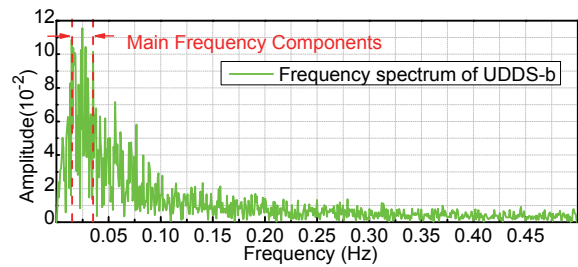Fig. 13. Charge counting accuracy at different sampling frequencies.

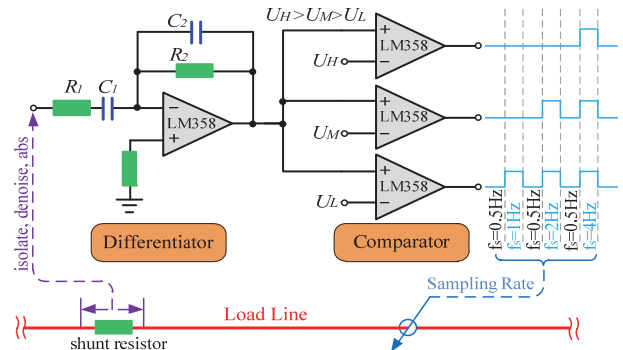Fig. 14. Frequency spectrum distribution of the UDDS-b profile.

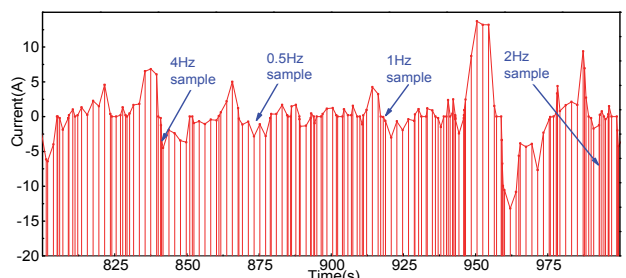Fig. 15. FA current sampling solution.

Fig. 16. Typical example of the sampled current by the frequency-adjustable sampling solution.
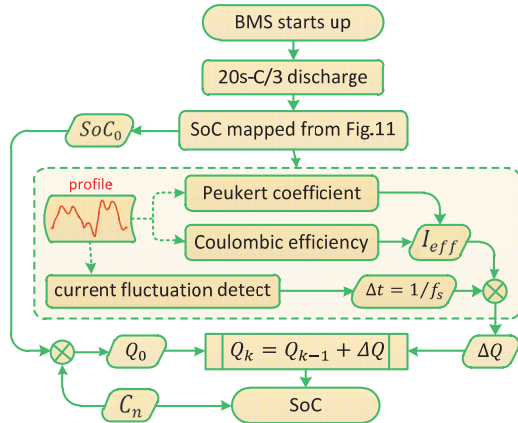
Fig. 17. Schematic of the SoC estimation scheme proposed, where Q_k is the remaining capacity at time step k.

isolation, amplification, denoising, and modulus) [38]. Then, the output magnitude, which represents the degree of current change, is compared with three thresholds ($U_H > U_M > U_L$) through comparators. The output pulses of the respective comparators indicate different current changing degrees, which are divided into three levels. The embedded μ processor detects these pulses, distinguishes the level, and then adjusts the sampling frequency. When the current fluctuates slightly, a low sampling frequency is adopted, and more idle time can be saved for other missions. When the current changes dramatically, a high frequency is applied. Fig. 16 presents an example of the sampled current. Nevertheless, high sampling frequency produces a sudden increase in data, which probably cannot be processed in time by the limited processing capability. Herein, the time-stamped data will be stored in a queue for handling in the subsequent idle time. Together with the enhanced Ah method in Section III, a global view of the SoC estimation scheme is outlined in Fig. 17.

V. RESULTS AND DISCUSSIONS

Verification experiments are carried out under the augmented UDDS-b profile with discharge peaks scaled to $3C$ and charge peaks scaled to $1C$. First, the FA sampling solution and the SoC mapping approach are evaluated. Then, the enhanced Ah method is verified under various temperatures. To assess the method generalization capability, estimations are carried out on Battery1 and Battery2. Prior to experiments, the batteries are fully charged and subsequently, as appropriate, discharged to a certain depth-of-discharge (DoD) at $C/3$ under 23 °C to create different initial SoCs. The reference SoC is obtained by post-processing the recorded data, that is, integrating the current from the end moment back to the start moment.

A. FA Sampling

First, the FA sampling is compared with three frequency-fixed samplings at 1, 2, and 4 Hz. Ten augmented UDDS-b

TABLE V
CHARGE COUNTING PERFORMANCE BY DIFFERENT SAMPLING SOLUTIONS

Solution	Sampling number	Final error(%)	
		Battery1	Battery2
FA sampling	47,335	0.38	0.44
1 Hz sampling	17,291	0.89	0.94
2 Hz sampling	34,581	0.58	0.68
4 Hz sampling	69,161	0.28	0.32
3.44 Hz sampling	59,502	0.38	0.42
2.74 Hz sampling	47,324	0.46	0.54

TABLE VI
SoC DETERMINATION PERFORMANCE DURING THE AVAILABLE SYSTEM IDLES IN UDDS TIME–VELOCITY REGIME

Time (s)	SoC error (%)			
	Battery1		Battery2	
	−5 ℃	30 ℃	−5 ℃	30 ℃
0–20	0.63	0.51	0.48	0.44
125–163	0.53	0.52	0.48	0.42
620–645	0.52	0.43	0.41	0.42
1023–1052	0.62	0.49	0.43	0.43
1313–1337	0.41	0.45	0.41	0.44

cycles are played, and the charge throughput is accumulated with the four sampling solutions. As tabulated in Table V, the error of the FA sampling is suppressed to 0.38%/0.44%, which is slightly higher than that of the 4 Hz sampling (0.28%/0.32%), but much smaller than the 1 Hz (0.89%/0.94%) and 2 Hz sampling (0.58%/0.68%).

Then, the frequency-fixed sampling is adjusted to reach the accuracy level of the FA sampling. When the frequency is 3.44 Hz, the error is 0.38%/0.42% with 59,502 samples, in contrast to the 47,335 samples of FA sampling. Consequently, the FA sampling can reduce the computational burden by approximately (59,502−47,335)/47,335=26% but achieve the same accuracy.

Afterward, the frequency-fixed sampling is changed to 2.74 Hz, and 47,324 samples are obtained (near the 47,335 of the FA-sampling), while the error increases to 0.46%/0.54%, in contrast to 0.38%/0.44% of the FA sampling. Consequently, given equal computing power, the FA sampling can improve the accuracy by approximately ((0.46−0.38)/0.38 +(0.54−0.44)/0.44)/2 = 22%.

B. SoC Determination during System Idles

In the original UDDS time–velocity regime in Fig. 12, five available system idles exist, where the time of zero velocity is longer than 20 s. During these idles, the proposed SoC determination approach in Section III.C is verified under two temperatures, −5 °C and 30 °C, on Battery1 and Battery2. As listed in Table VI, the determination errors suggest that the SoC determination approach works well.

C. SoC Estimation under Constant Temperature

Comparative experiments are arranged under constant temperatures. The batteries are soaked in the thermal chamber for five hours to achieve steady temperature states before the experiments. Then, several augmented UDDS-b cycles are applied on the fully charged batteries until the lower cut-off voltage is reached.

$$\bar{\eta} = \frac{\sum \eta(SoC, I_n, T)}{19}, SoC = 5, 10, 15, \cdots, 95\% \quad (21)$$

where I_n is the reference current and T is the battery temperature. In addition, the denominator capacity that corresponds to T is obtained by Eq. (10).

The estimation results of the enhanced Ah method (Enh-Ah) and the simple Ah method (Simp-Ah) are shown in Fig. 18. For Battery1 and Battery2, the Max SoC errors under different temperatures occur at the end of the discharging process due to the accumulation effect. Expectedly, the Max errors of Enh-Ah, as low as 1.90%/1.74% for Battery1 and 2.09%/1.57% for Battery2, are guaranteed to be smaller than those of Simp-Ah, which reach 4.56%/5.47% for Battery1 and 4.23%/5.78% for Battery2. The errors of Simp-Ah under 40 °C and –7 °C evolve with nearly the same slope. As for Enh-Ah, the error growth rates under low temperature are greater than those under high temperature. The reasons for the inferior performance of Simp-Ah to Enh-Ah are as follows:

- The average Coulombic efficiency $\bar{\eta}$ cannot represent the varying $\eta(SoC, I, T)$ well.
- The effect of discharging efficiency is not considered.
- $\bar{\eta}$ is calculated for a specific temperature, while the actual temperature undergoes obvious fluctuations.

The estimation accuracy under normal temperature (40 °C) is clearly higher than that under extreme temperature (–7 °C). The considerable difference between the released capacities under 40 °C and –7 °C implies that Battery2 is more sensitive to temperature and suffers serious capacity degradation under low temperature. This finding may be ascribed to the package and shape of Battery2, which contribute to heat dissipation. Constant temperature experiments produce satisfactory results, which suggest that the proposed Enh-Ah estimator is superior to the traditional Simp-Ah estimator.

D. SoC Estimation under Varying Temperatures

To analyze the robustness of the Enh-Ah estimator against harsh conditions, comprehensive experiments are carried out with the temperature varying within the main range specified in Table I. The temperature varies from –13℃ to 37℃ for Battery1 and from –2℃ to 45 ℃ for Battery2. Given that Simp-Ah has no coping mechanism against the varying temperature, which leads to a meaningless estimation result, the comparative experiments by Simp-Ah are omitted in this section. For Battery1 and Battery2, estimations are performed from two initial states: the fully charged state and a partially
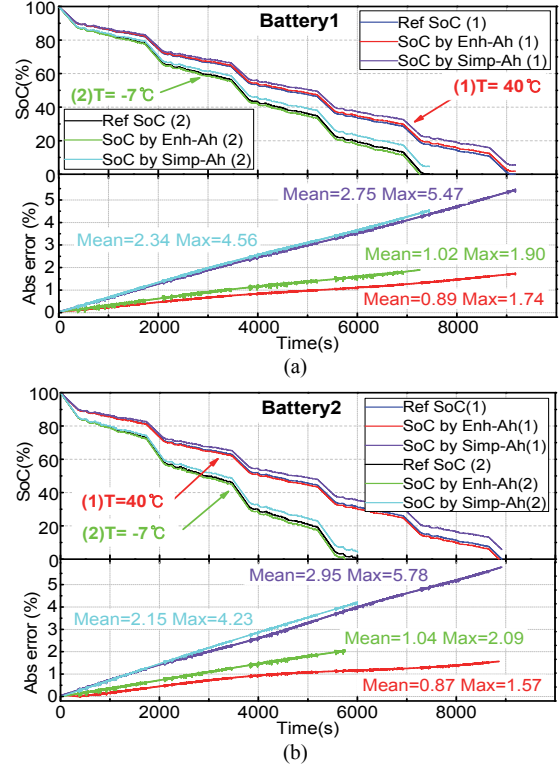

Fig. 18. Performance comparison between the Enh-Ah estimator and the Simp-Ah estimator under constant ambient temperatures (40 ℃ and –7 ℃) on (a) Battery1 and (b) Battery2.
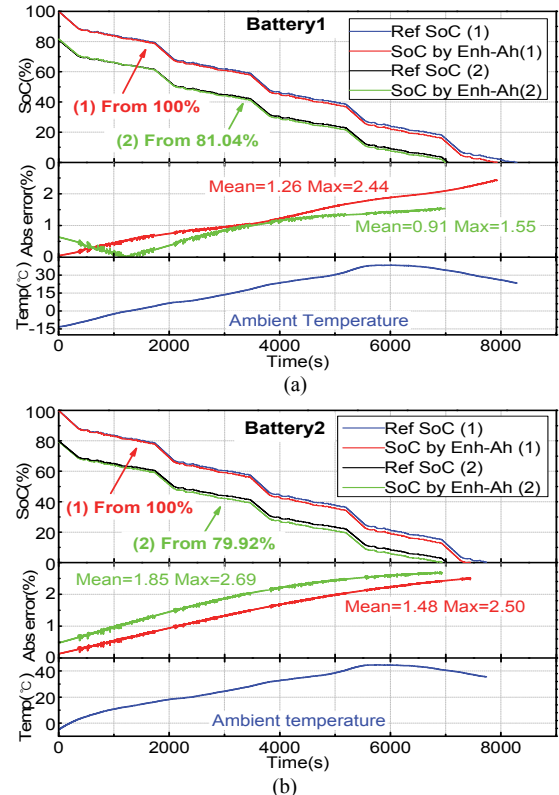

Fig. 19. Performance of the proposed Enh-Ah estimator under varying ambient temperatures on (a) Battery1 (–13 °C–37°C) and (b) Battery2 (–2 °C–45 °C).

discharged state. For example, the initial SoC of the partially discharged state for Battery1 is obtained by first discharging the battery to approximately 20% DoD and then mapping from Fig. 11 using the real-time discharging terminal voltage and temperature.

Fig. 19 shows that the SoCs estimated by Enh-Ah can follow the reference SoCs closely. Though subject to varying temperature, the Max errors remain lower than 2.69%, part of which is ascribed to the initial errors in the partially discharged cases. In summary, the proposed Enh-Ah SoC estimator maintains high accuracy in the entire temperature range.

VI. CONCLUSIONS

An enhanced Ah method for SoC estimation is proposed by combining *Peukert's* law for the discharging process and the Coulombic efficiency for the charging process. However, the *Peukert* coefficient and Coulombic efficiency measured under a particular condition are unsuitable for dynamic load and varying temperature. This paper proposes a concept of effective current factoring in the impact of current rate and temperature on capacity. The difference in charge counting accuracy at different sampling frequencies is analyzed. In response, a FA current sampling solution is devised. Consequently, a SoC estimator of low complexity and low computational overhead but high accuracy is established. Experiments using dynamic load profile and various temperature profiles on two batteries of different chemistries verify the effectiveness and robustness of the proposed SoC estimation method.

APPENDIX

A. Derivation of Eq. (5)

For current rate I, the corresponding effective current $I_{eff}(I)$ with respect to the nominal capacity C_n means that

$$C_a/I = C_n/I_{eff} = t \qquad (A1)$$

where t is the time spent to deplete the battery at rate I, and C_a is the corresponding released charge.

From Eq. (1), we know that

$$I^{pc} \cdot t = I_n{}^{pc} \cdot t_n \qquad (A2)$$

where I_n is the nominal discharge rate regarding C_n, and t_n is the corresponding discharge time.

Transformed from Eq. (A. 2), we obtain

$$C_a/C_n = (I_n/I)^{pc-1} \qquad (A3)$$

where $C_a = I \cdot t$ and $C_n = I_n \cdot t_n$.

Then, by arranging Eq. (A. 1), we obtain

$$I_{eff} = I \cdot C_n/C_a. \qquad (A4)$$

When Eq. (A. 3) is substituted into Eq. (A. 4), Eq. (5) can be obtained as

$$I_{eff} = I \cdot (I/I_n)^{pc-1}. \qquad (A5)$$

B. Derivation of Eq. (6)

Q_a and Q_b are the corresponding capacities of I_n and I, respectively, and by substituting them into Eq. (A. 3), we obtain

$$Q_b/Q_a = (I_n/I)^{pc-1}. \qquad (B1)$$

A logarithmic expression can be derived as

$$pc - 1 = log_{I_n/I}(Q_b/Q_a). \qquad (B2)$$

According to the logarithmic formula of Change of Base, Eq. (B2) is re-expressed as

$$pc = 1 + ln(Q_b/Q_a)/ln(I_n/I). \qquad (B3)$$

REFERENCES

[1] C. Zhang, K. Li, L. Pei, and C. Zhu, "An integrated approach for real-time model-based state-of-charge estimation of lithium-ion batteries," *J. Power Sources*, Vol. 283, pp. 24-36, Jun. 2015.

[2] K. S. Ng, C-S Moo, Y-P Chen, and Y-C Hsieh, "Enhanced coulomb counting method for estimating state-of-charge and state-of-health of lithium-ion batteries," *Applied Energy*, Vol. 86, No. 9, pp. 1506-1511, Sep. 2009.

[3] Y. He, X. Liu, C. Zhang, and Z. Chen, "A new model for State-of-Charge (SOC) estimation for high-power Li-ion batteries," *Applied Energy*, Vol. 101, pp. 808-814, Jan. 2013.

[4] L. Lavigne, J. Sabatier, J. M. Francisco, F. Guillemard, and A. Noury, "Lithium-ion Open Circuit Voltage (OCV) curve modelling and its ageing adjustment," *J. Power Sources*, Vol. 324, pp. 694-703, Aug. 2016.

[5] G. Dong, J. Wei, C. Zhang, and Z. Chen, "Online state of charge estimation and open circuit voltage hysteresis modeling of LiFePO4 battery using invariant imbedding method," *Applied Energy*, Vol. 162, pp. 163-171, Jan. 2016.

[6] L. Gao, S. Liu, and R. A. Dougal, "Dynamic lithium-ion battery model for system simulation," *IEEE Trans. Compon. Packag. Technol.*, Vol. 25, No. 3, pp. 495-505, Sep. 2002.

[7] F. Feng, R. Lu, and C. Zhu, "A combined state of charge estimation method for lithium-ion batteries used in a wide ambient temperature range," *Energies*, Vol. 7, No. 5, pp. 3004-3032, 2014.

[8] Y. Zheng, M. Ouyang, and L. Lu, "Study on the correlation between state of charge and Coulombic efficiency for commercial lithium ion batteries," *J. Power Sources*, Vol. 289, pp. 81-90, Sep. 2015.

[9] W. Waag, S. Käbitz, and D. U. Sauer, "Experimental investigation of the lithium-ion battery impedance characteristic at various conditions and aging states and its influence on the application," *Applied Energy*, Vol. 102, pp. 885-897, Feb. 2013.

[10] L. Lu, X. Han, J. Li, J. Hua, and M. Ouyang, "A review on the key issues for lithium-ion battery management in electric vehicles," *J. Power Sources*, Vol. 226, pp. 272-288, Mar. 2013.

[11] W. Waag, C. Fleischer, and D. U. Sauer, "Critical review of the methods for monitoring of lithium-ion batteries in electric and hybrid vehicles," *J. Power Sources*, Vol. 258,

pp. 321-339, Jul. 2014.

[12] A. Fotouhi, D. J. Auger, and K. Propp, "A review on electric vehicle battery modelling: From Lithium-ion toward Lithium–Sulphur," *Renew. Sustain. Energy Rev.*, Vol. 56, pp. 1008-1021, Apr. 2016.

[13] F. Yang, Y. Xing, D. Wang, and K-L Tsui, "A comparative study of three model-based algorithms for estimating state-of-charge of lithium-ion batteries under a new combined dynamic loading profile," *Applied Energy*, Vol. 164, pp. 387-399, Feb. 2016.

[14] H. He, R. Xiong, H. Guo, and S. Li, "Comparison study on the battery models used for the energy management of batteries in electric vehicles," *Energy Convers. Manag.*, Vol. 64, pp. 113-121, Dec. 2012.

[15] M. Berecibar, I. Gandiaga, I. Villarreal, N. Omar, J. Van Mierlo, and P. Van den Bossche, "Critical review of state of health estimation methods of Li-ion batteries for real applications," *Renew. Sustain. Energy Rev.*, Vol. 56, pp. 572-587, Apr. 2016.

[16] Z. Chen, Y. Fu, and C. C. Mi, "State of charge estimation of lithium-ion batteries in electric drive vehicles using extended Kalman filtering," *IEEE Trans. Veh. Technol.*, Vol. 62, No. 3, pp. 1020-1030, Mar. 2013.

[17] W. Zhang, W. Shi, and Z. Ma, "Adaptive unscented Kalman filter based state of energy and power capability estimation approach for lithium-ion battery," *J. Power Sources*, Vol. 289, pp. 50-62, Sep. 2015.

[18] J. Xie, J. Ma, Y. Sun, and Z. Li, "Estimating the state-of-charge of lithium-ion batteries using an H-infinity observer with consideration of the hysteresis characteristic," *J. Power Electron.*, Vol. 16, No. 2, pp. 643-653, Mar. 2016.

[19] A. Tulsyan, Y. Tsai, R. B. Gopaluni, and R. D. Braatz, "State-of-charge estimation in lithium-ion batteries: A particle filter approach," *J. Power Sources*, Vol. 331, pp. 208-223, Nov. 2016.

[20] A. Hausmann and C. Depcik, "Expanding the Peukert equation for battery capacity modeling through inclusion of a temperature dependence," *J. Power Sources*, Vol. 235, pp. 148-158, Aug. 2013.

[21] L. Zheng, L. Zhang, J. Zhu, G. Wang, and J. Jiangd, "Co-estimation of state-of-charge, capacity and resistance for lithium-ion batteries based on a high-fidelity electrochemical model," *Applied Energy*, Vol. 180, pp. 424-434, Oct. 2016.

[22] L. Kang, X. Zhao, and J. Ma, "A new neural network model for the state-of-charge estimation in the battery degradation process," *Applied Energy*, Vol. 121, pp. 20-27, May 2014.

[23] C. Hametner, and S. Jakubek, "State of charge estimation for Lithium Ion cells: Design of experiments, nonlinear identification and fuzzy observer design," *J. Power Sources*, Vol. 238, pp. 413-421, Sep. 2013.

[24] J. N. Hu, J. J. Hu, H. Lin, X. P.Li, C. L. Jiang, X. H. Qiu, and W. S. Lia, "State-of-charge estimation for battery management system using optimized support vector machine for regression," *J. Power Sources*, Vol. 269, pp. 682-693, Dec. 2014.

[25] L. Gold, T. Bach, W. Virsik, A. Schmitt, J. Müller, T. E.M. Staab, and Gerhard Sextl, "Probing lithium-ion batteries' state-of-charge using ultrasonic transmission –Concept and laboratory testing," *J. Power Sources*, Vol. 343, pp. 536-544, Mar. 2017.

[26] J. Cannarella, and C. B. Arnold, "State of health and charge measurements in lithium-ion batteries using mechanical stress," *J. Power Sources*, Vol. 269, pp. 7-14, Dec. 2014.

[27] J. Tinnemeyer, "New advances in lithium ion battery monitoring," *Battery Power Conference*, pp. 19-20, Oct. 2010.

[28] L. Zhao, M. Lin, and Y. Chen, "Least-squares based coulomb counting method and its application for state-of-charge (SOC) estimation in electric vehicles," *International Journal of Energy Research*, Vol. 40, No. 10. pp. 1389-1399, Mar. 2016.

[29] W. Peukert, "Über die Abhängigkeit der Kapazität von der Entladestromstärke bei Bleiakkumulatoren," *Elektrotechnische Zeitschrift*, Vol. 20, pp. 20-21, 1897.

[30] D. Baert and A.Vervaet, "Lead-acid battery model for the derivation of Peukert's law," *Electrochimica acta*, Vol. 44, No. 20, pp. 3491-3504, Jun. 1999.

[31] D. Doerffel and S. A. Sharkh, "A critical review of using the Peukert equation for determining the remaining capacity of lead-acid and lithium-ion batteries," *J. Power Sources*, Vol. 155, No. 2, pp. 395-400, Apr. 2006.

[32] N. Omar, P. V. Bossche, T. Coosemans, and J. V. Mierlo, "Peukert revisited – Critical appraisal and need for modification for lithium-ion batteries," *Energies*, Vol. 6, No. 11, pp. 5625-5641, 2013.

[33] J. R. Belt, "Battery test manual for plug-in hybrid electric vehicles," *Idaho National Laboratory (INL)*, 2010.

[34] D. Rakhmatov, S. Vrudhula, and D. A.Wallach, "A model for battery lifetime analysis for organizing applications on a pocket computer," *IEEE Trans. Very Large Scale Integr. (VLSI) Syst.*, Vol. 11, No. 6, PP. 1019-1030, Dec. 2003.

[35] M. Thele, O. Bohlen, D. U. Sauer, and E. Karden, "Development of a voltage-behavior model for NiMH batteries using an impedance-based modeling concept," *J. Power Sources*, Vol. 175, No. 1, pp. 635-643, Jan. 2008.

[36] M. A. Roscher, and D. U. Sauer, "Dynamic electric behavior and open-circuit-voltage modeling of LiFePO4-based lithium ion secondary batteries," *J. Power Sources*, Vol. 196, No. 1, pp. 331-336, Jan. 2011.

[37] United States Advanced Battery Consortium, "Electric vehicle battery test procedures manual," *USABC*, Jan. 1996.

[38] J. G. Graeme, G. E. Tobey, and L. P. Huelsman, "Operational amplifiers. Design and applications," *Burr-Brown Research Corporation*, pp. 218-220, 1971.
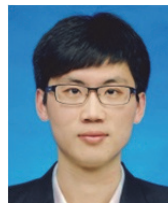
Jiale Xie received his B.S. degree from Harbin Engineering University, Harbin, China, in 2010, and his M.S. degree in Control Science and Engineering from the Harbin Institute of Technology, Harbin, China, in 2012. From 2012 to 2013, he worked with the Envision Energy Co., Ltd., Shanghai, China, where he was in charge of the control strategy of wind turbines. Since 2014, he has been working toward his Ph.D. degree at the School of Astronautics, Harbin Institute of Technology. His current research interests include battery modeling and simulation, state estimation of power Li-ion batteries, series battery string equalization, and embedded control.

Jiachen Ma was born in 1964, China. He received his B.S., M.S. and Ph.D. degrees in Control Science and Engineering from the Harbin Institute of Technology, Harbin, China, in 1985, 1988 and 2006 respectively. He is currently a professor at the School of Astronautics, Harbin Institute of Technology. His current research interests include intelligent robots, precise machine vision detection, embedded system and application, and battery energy management.

Kun Bai received his B.S. and M.S. degrees in Control Science and Engineering from Harbin Engineering University, Harbin, China, in 2010 and 2013, respectively. Since 2013, he has worked with the State Grid Jibei Electric Power Co. Ltd., Maintenance Branch, Beijing, China, where he is in charge of power grid failure diagnosis. His current research interests include high-voltage insulation, smart power grids, and wind–solar-storage hybrid power system.